Check for updates

Polymorphism of garnet solid electrolytes and its implications for grain-level chemo-mechanics

Marm B. Dixit[1,2 ✉], Bairav S. Vishugopi[3], Wahid Zaman[1,4], Peter Kenesei[5], Jun-Sang Park[5], Jonathan Almer[5], Partha P. Mukherjee[3] and Kelsey B. Hatzell [1,6,7 ✉]

Understanding and mitigating filament formation, short-circuit and solid electrolyte fracture is necessary for advanced all-solid-state batteries. Here, we employ a coupled far-field high-energy diffraction microscopy and tomography approach for assessing the chemo-mechanical behaviour for dense, polycrystalline garnet ($Li_7La_3Zr_2O_{12}$) solid electrolytes with grain-level resolution. In situ monitoring of grain-level stress responses reveals that the failure mechanism is stochastic and affected by local microstructural heterogeneity. Coupling high-energy X-ray diffraction and far-field high-energy diffraction microscopy measurements reveals the presence of phase heterogeneity that can alter local chemo-mechanics within the bulk solid electrolyte. These local regions are proposed to be regions with the presence of a cubic polymorph of LLZO, potentially arising from local dopant concentration variation. The coupled tomography and FF-HEDM experiments are combined with transport and mechanics modelling to illustrate the degradation of polycrystalline garnet solid electrolytes. The results showcase the pathways for processing high-performing solid-state batteries.

Solid-state batteries offer the opportunity to leverage energy-dense metallic anodes and high-voltage cathodes to achieve safe, durable and affordable secondary energy storage systems[1,2]. However, unfavourable electro-chemo-mechanical dynamics can contribute to non-optimal material utilization, mechanical degradation and poor ion transport[1,3–6]. In particular, reversible lithium (Li)-metal electrodeposition and dissolution remains a notable challenge, limiting the adoption of Li-metal solid-state batteries[3,7–11]. Non-uniform interfaces (for example, voids/delamination), interphase growth and current focusing can accelerate degradation[12,13]. A wide range of solid electrolyte materials including garnets[14], thiophosphates[13], argyrodites[15] and anti-perovskites[16] experience filament formation and shorting at low current densities ($\leq 10\,mA\,cm^{-2}$). Unravelling the role that material heterogeneity (interface and bulk) has on filament formation is critical towards engineering materials for next-generation batteries[7,8].

Garnet-type $(A_3B_2(XO_4)_3)$ solid electrolytes possess high ionic conductivity and good electrochemical stability against Li-metal electrode[14]. These ceramics have a Young's modulus of >50 GPa and shear modulus of ~60 GPa (refs. [17–20]). $Li_7La_3Zr_2O_{12}$ (LLZO) exhibits two structures: low-temperature (<700 °C) tetragonal symmetry with low ionic conductivity and high-temperature (>700 °C) cubic structure with high ionic conductivity[21–23]. Aliovalent substitution of Ta, Ga and Al into this matrix can help stabilize the cubic phase at low temperatures[21,24]. Recent results suggest that the kinetics of Li electrode at garnet interfaces is very high and may be able to sustain currents $\geq 100\,mA\,cm^{-2}$ (ref. [25]). However, most experimental studies report failure below $1\,mA\,cm^{-2}$. The discrepancy in performance is probably due to an ensemble of microstructural properties (grains, grain boundaries and voids/defect) and chemical inhomogeneities[19,26–28].

Polycrystalline garnet solid electrolytes exhibit both structural and chemical inhomogeneity that can affect performance. LLZO can undergo phase transformation from cubic to tetragonal when in contact with Li metal (anode)[29] and $LiCoO_2$ (cathode)[30]. The tetragonal phase is chemically identical to the cubic phase but has a lower ionic conductivity and can impact electrode kinetics[30]. Chemical inhomogenities also exist as a result of dopant diffusion to grain boundaries during processing. This can impact the mechanical properties of the grain boundary and chemical stability of the electrolyte[31]. Although there have been numerous local measurement tools (for example, electron holography and transmission electron microscopy)[32,33] used to observe grain-specific transport properties, the direct interrogation of grain-level chemo-mechanics during in situ operation has been elusive to the community due the lack of time- and space-resolved techniques that are capable of accessing these buried interfaces. Techniques that combine tomography and rotating-crystal-method-based diffraction methods (for example, high-energy diffraction microscopy) can spatially resolve the microstructure and local micromechanical states[34–39]. Far-field high-energy diffraction microscopy (FF-HEDM) is a variant of this technique and can measure the full elastic strain tensor on a grain-by-grain basis in bulk samples[37,40]. In a typical FF-HEDM experiment, the sample is rotated from –180.0° to 180.0° with respect to the incoming X-rays at 0.1° steps (Fig. 1b and Supplementary Figs. 1 and 2). Diffraction images are captured on a two-dimensional area detector and can be processed to track the grain centre of mass, crystallographic orientations, sizes and lattice strain tensor information for each grain inside a polycrystalline sample (Fig. 1a).

In this work, we combine FF-HEDM with X-ray tomography measurements to track mesoscale microstructural transformations in garnet-type LLZO during in situ conditions. FF-HEDM can quantify and track stress evolution at the individual-grain level during electrochemical cycling. Combining this technique with direct

[1]Department of Mechanical Engineering, Vanderbilt University, Nashville, TN, USA. [2]Electrification and Energy Infrastructures Division, Oak Ridge National Laboratory, Oak Ridge, TN, USA. [3]School of Mechanical Engineering, Purdue University, West Lafayette, IN, USA. [4]Department of Mechanical and Aerospace Engineering, Princeton University, Princeton, NJ, USA. [5]Advanced Photon Source, Argonne National Laboratory, Lemont, IL, USA. [6]Andlinger Center for Energy and the Environment, Princeton University, Princeton, NJ, USA. [7]Present address: Department of Mechanical and Aerospace Engineering, Princeton University, Princeton, NJ, USA. ✉e-mail: dixitmb@ornl.gov; kelsey.hatzell@princeton.edu
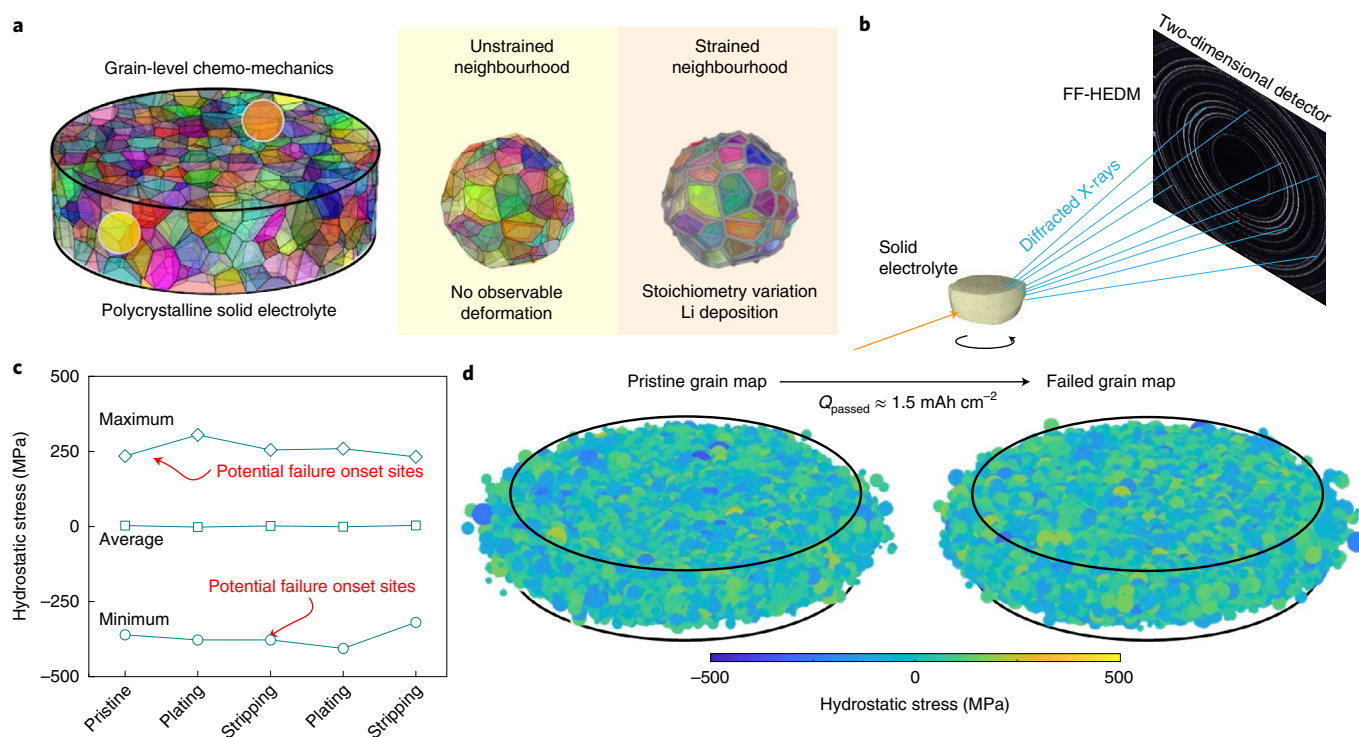
Fig. 1 | Mechanical response of a polycrystalline LLZO material. a, Schematic showing a polycrystalline pellet and the associated strained and unstrained neighbourhoods. The different colours represent the individual grains with differing orientations within the solid electrolyte. Under normal conditions, the local neighbourhood comprises different grain boundaries and voids that represent the 'unstrained condition' for this study. On extended electrochemical cycling, local stoichiometric variations, Li deposition and crack formation can lead to mechanical stresses that alter the mesoscale structure of the solid electrolyte. **b**, Schematic showing the FF-HEDM technique. The orange arrow directed towards the sample from the left represents high-energy monochromatic X-rays, whereas the blue arrows emerging from the solid electrolyte are the diffracted X-ray beams. **c**, Hydrostatic stress evolution during cycling of the Li|LLZO|Li sample. The stress values are averaged over all the grains in the measured sample. The maximum and minimum values are shown for individual grains in the sample. Note that the red arrows depict the regions of minimum and maximum stress within the pellet, which are potential sites for failure onset. **d**, Three-dimensional grain maps for the pristine and failed sample. The grains are colour mapped to the hydrostatic stress values. The two circles are drawn over the scatter plot to help in visualization of the solid electrolyte shape. A total of 1.5 mAh cm^{-2} Li is cycled before failure. The grain map is visualized for the entire LLZO pellet (diameter, ~1.6 mm; thickness, ~1.0 mm).

imaging approaches (for example, tomography) enables the simultaneous measurements of structure from the angstrom to millimetre scale. Tomography is critical for linking nanoscale stress transformations to mesoscale material transformation pathways (for example, porosity changes, filament formation and fracture). This work provides fundamental insights into the role played by structural heterogeneity on material transformation pathways of solid electrolytes. In particular, filament formation is shown to occur in solid electrolyte regions with high concentrations of polymorphic phases. Engineering solid-state batteries for high-rate, energy-dense applications requires simultaneous control over mesoscale structural and chemical inhomogeneities.

Chemo-mechanical response of polycrystalline solid electrolytes

Symmetric Li|LLZO|Li cells were cycled at the Advanced Photon Source in a custom-made cell holder (Supplementary Fig. 3a). The polarization profile is relatively flat during the first plating cycle, indicating reversible Li electrodeposition. The polarization profile begins to slope upwards at high current densities, which is consistent with void formation (Supplementary Fig. 3b). In situ tomography and FF-HEDM measurements were conducted after each stripping and plating experiments up until failure (~1.5 mAh cm^{-2}) (ref. [41]). Approximately 30,000 grains were measured within the pellet (diameter, 2 mm) and grain sizes ranged between 55 and 60 μm.

FF-HEDM calculates the full strain tensor for individual grains via indexing (Supplementary Information). The corresponding stress tensor is calculated by assuming a cubic lattice and employing the elastic modulus established for Al-doped LLZO obtained from first-principles calculations[42]. Hydrostatic stress is the average of the normal stresses acting on the grain, whereas von Mises stress provides insights into the shear stresses acting on the material. Due to the underlying assumptions regarding the stress and strain distribution (isotropic), the absolute values are not directly employed. However, the relative trends provide insights into the grain-level chemo-mechanics.

The average hydrostatic and von Mises stress values show negligible variation during cycling across ~30,000 grains (Fig. 1c,d and Supplementary Figs. 4 and 6). However, the minimum and maximum hydrostatic stress measurements show some changes between the stripping and plating steps (Fig. 1c). These results were also validated on an additional sample (Supplementary Figs. 4a and 5). The grain-specific stress distribution is visualized as violin plots (Fig. 2a,b and Supplementary Fig. 5). These plots represent the statistical variability in stress (hydrostatic and von Mises) across all the grains (Fig. 2a,b and Supplementary Fig. 5). Most grains do not experience any change in hydrostatic stress during electrochemical cycling. However, a minority of grains demonstrate changes in the mean stress during cycling. This suggests the existence of local heterogeneities within the polycrystalline garnet oxides. Examples of
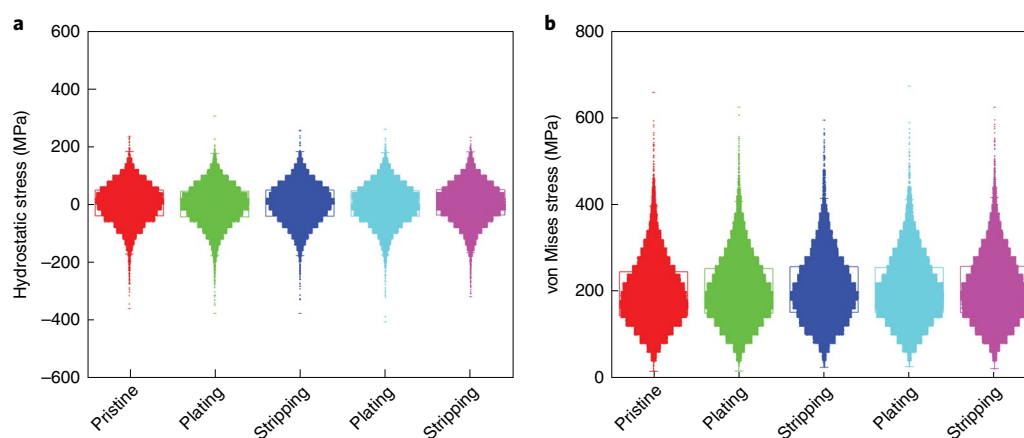
Fig. 2 | Stress response of polycrystalline LLZO material. a,b, Violin plots depicting the overall stress distribution along with the individual datasets for hydrostatic stress (**a**) and von Mises stress (**b**). The width of the violin plots indicates the number density of grains at the specified stress value.

heterogeneity include (1) grains, (2) grain boundaries, (3) defects and (4) secondary phases. The implications of these heterogeneities can be observed via mapping grain measurements in three dimensions (Fig. 1d and Supplementary Fig. 4). Figure 1d demonstrates how hydrostatic stress varies between grains in an entire pellet before and after electrochemical cycling experiments. The high degree of variability in both space and time reveals the importance of microstructural heterogeneities on the mechanical response of these material systems (Supplementary Fig. 7).

Evaluation of secondary phases in bulk LLZO

FF-HEDM and high-resolution X-ray diffraction (XRD) experiments (Fig. 1 and Extended Data Fig. 1a–c) reveal the presence of two different cubic phases within the LLZO solid electrolyte: (1) a majority 220 space group (I–$43d$) (~30,000 grains) and (2) a minority 230 space group (Ia–$3d$) (~1,000 grains) (Fig. 3a and Supplementary Fig. 8). Both space groups are cubic but have different Li coordination sites (Fig. 3a). Mesoscale models based on the kinetic Monte Carlo algorithm and finite element method have been developed to understand the implications of the secondary phase on local ion transport and mechanical response of the solid electrolyte (Supplementary Information)[43,44]. Ions can experience transport gradients within a solid electrolyte because each polymorph (220 and 230) has a different activation energy. Our simulation assumes an ion-migration-barrier offset of around 0.06 eV between the two phases. Figure 3b demonstrates a theoretical domain where the centre region is a 7 nm secondary phase (minority phase, 230) in contact with a 220 space group. Here i/i_0 represents the occupancy descriptor, and is normalized with respect to the initial ion occupancy (i_0). An initial ion occupancy of 2% is assumed throughout the domain. Local occupancy of Li ions is visualized in the domain after 4×10^8 migration events (Fig. 3b). Li ions migrate to domains with lower activation barriers (220 space group). Thus, regions with the 230 space group exclude Li ions, which results in more tortuous ion transport pathways and spatially distinct regions with directed ion transport.

Finite element method simulations were carried out to probe the solid electrolyte's electrical and mechanical response (Supplementary Information provides the model details). For an externally applied pressure of 1 MPa and an applied current density of 0.5 mA cm^{-2}, notable gradients in both stress and electric potentials are observed close to the secondary phase regions (Fig. 3c,d). Additionally, the local ion occupation and electric potential response are evaluated for the case where the secondary phase is more conductive than the primary domain (Supplementary Fig. 10). Even for this case,

a distinct ion occupation and electric potential response in the vicinity of the secondary phase is observed. Isolated instances of the 230 space group within the bulk material are inferred to be a major cause for the onset of heterogeneity in mechanical and ion transport response within the solid electrolyte pellet.

Symmetry reduction from Ia–$3d$ to I–$43d$ (Fig. 3a and Extended Data Fig. 1a–c) can occur as a result of chemical ion exchange (Li$^+$ with H$^+$)[45,46], cation ordering on specific sites[24] and mechanical effects during processing. It is possible that mechanical milling as well as local dopant variation can result in the two phases observed within the solid electrolyte (Extended Fig. 1a–c). The limited distinct reflections between the 220 and 230 space groups have very low structure factors, making their detection difficult (Supplementary Fig. 11). Spatially resolved high-resolution XRD studies were carried out at the Advanced Photon Source (Extended Data Fig. 1) to resolve the low structure factor peaks. A PILATUS detector enables the measurement of a unique <141> reflection for the 230 space group (Extended Data Fig. 1c). This reflection varies in intensity throughout the sample depth, indicating a heterogeneous distribution within the sintered pellet. Refinement of the XRD data reveals that the 230 space group accounts for ~10% of all grains (Supplementary Fig. 12).

Evaluating the spatial distribution of stress response for each distinctive grain among the ≥30,000 grains is challenging. Here we implement an unsupervised machine learning algorithm (k-means) that segregates the input data into k number of individual clusters based on the square errors between the individual data points. The k-means algorithm helps visualize the following in space: low-strain regions (yellow), medium-strain regions (blue) and high-strain regions (orange) in both pristine and failed samples (Fig. 4a and Supplementary Fig. 13a). The results indicate no preferential direction of strain evolution between the pristine and failed sample. A similar analysis was conducted during stripping and plating experiments to visualize stress evolution in situ (Supplementary Figs. 14 and 15). A majority of the grains do not show any deviation in the stress values as expected from the aggregate plots (Fig. 1c and Supplementary Fig. 4a). The absence of bulk-scale trends in stress distributions indicate that the failure of LLZO is potentially driven by a stochastic, isolated mechanism.

Tracking the onset and growth of failure mechanism

To probe this stochastic response, we labelled and tracked different locations within the pellet during cycling. The grains with the highest stress values were labelled as 'hot spots' and the grains with the lowest stress values were labelled as 'cold spots' (Fig. 4b,c
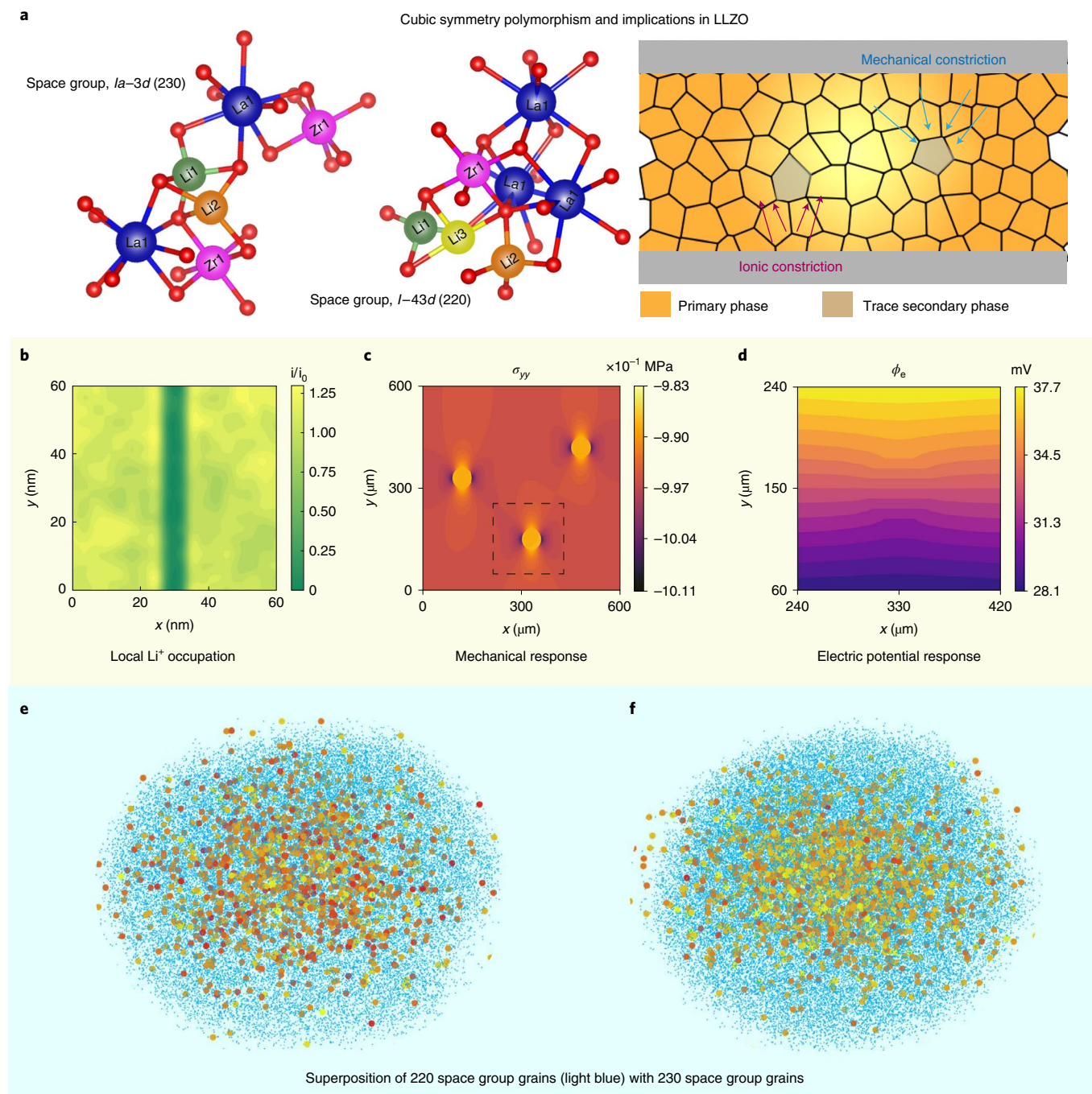
Fig. 3 | Local phase anisotropy in garnet solid electrolytes. a, Local Li coordination environment in LLZO with the 220 and 230 space groups. Schematic highlighting the mechanical and ionic constriction effects in pellets due to the presence of a trace secondary phase. **b**, Mesoscale modelling results, highlighting the variation in local Li$^+$ occupation due to the presence of a secondary phase with a distinct ion migration barrier compared with the bulk. **c,d**, Mechanical (**c**) and electric potential (**d**) responses of the solid electrolyte domain with the secondary phase. For the local ion occupation and electric potential response, the secondary phase is considered less conductive than the primary domain. **e,f**, Superposition of the 220 space group grains (light-blue colour) with the grains identified in the 230 space group for the pristine (**e**) and failed (**f**) sample.

and Supplementary Fig. 16). All the grains within ~100 μm of the hot and cold spots were tracked during cycling experiments to evaluate 'spatially' distinct neighbourhoods. Both hot- and cold-spot neighbourhoods experience an increase in hydrostatic stress after the initial plating experiment (Fig. 4b,c). The consistent build up of stresses between the pristine and plating steps suggests a transport-driven mechanism where lattice distortion of the grains leads to local increases in stress. The local hot/cold

spots are probably located at the secondary phases, which act as ion transport bottlenecks with gradients in ion occupancy and mechanical properties (Fig. 3c). These hot and cold spots were tracked over several cycles and similar trends were observed (Supplementary Figs. 17–22). Sample thickness, porosity (and local variation) and cell geometry can impact the stress response of a solid electrolyte[13]. We also evaluated the hydrostatic stress for each grain (≥30,000) as a function of the grain size at different
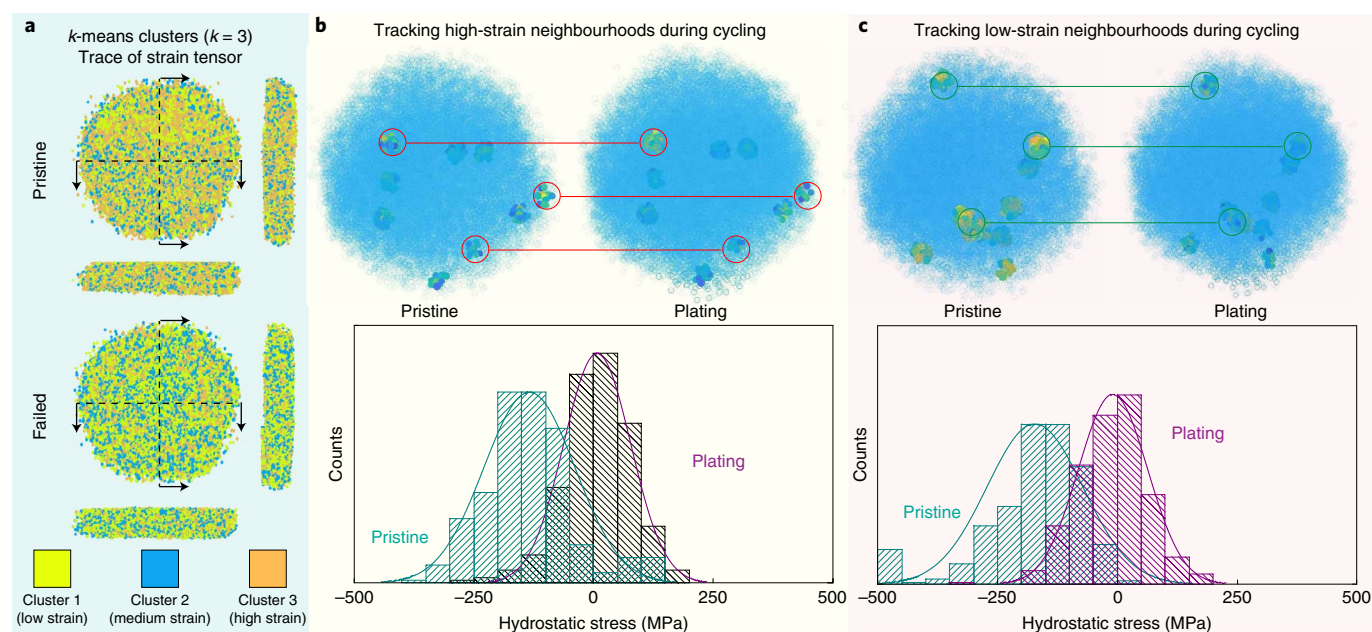
Fig. 4 | Hydrostatic stress evolution during cycling. a, Full pellet assessment for directional stress behaviour using unsupervised machine learning algorithm, *k*-means. No preferential spatial distribution for hydrostatic stress for individual grains is observed between the pristine and failed sample. **b,c**, Tracking of high-stress (**b**) and low-stress (**c**) neighbourhoods at two different stages of cycling—pristine and the first plating step—along with the corresponding histograms and normal distribution fitting for the hydrostatic stress value for the grains in the identified neighbourhood.

stages of electrochemical cycling (Supplementary Fig. 23). Larger grains demonstrate larger absolute stress values compared with smaller grains. Smaller grains have more grain boundaries, which may lead to faster stress relaxation[27,43,47].

Correlation of chemo-mechanics and bulk microstructure

Hot and cold neighbourhoods identified in the FF-HEDM dataset were directly mapped onto direct imaging experiments (for example, tomography). The grain maps (FF-HEDM) and tomography datasets were manually aligned and corrected for sample motion and rotations (Supplementary Fig. 24). Mapping grain-specific information to the tomographic data allows us to directly track material evolution (Li-metal growth) at the hot- and cold-spot locations by evaluating the X-ray-transparent region[8]. As Li grows into a solid electrolyte, the volume of the material that is transparent to X-rays increases. A 'hot spot' was monitored and is represented in Extended Fig. 2a. The 'change' in the local microstructure at a hot spot before and after failure is visualized in Extended Fig. 2a. It is evident that the local microstructure undergoes significant change on failure at the hot spot. The mechanical and ionic constrictions that can occur at these hot spots due to the secondary phase (Fig. 3) may be responsible for the observed high level of microstructure variation. A similar behaviour is observed across multiple hot/cold spots evaluated as well as across two distinct samples (Fig. 2b and Supplementary Fig. 9). The depth-averaged porosity variation value between the pristine and failed sample shows essentially no change in the unstrained regions and a large structural variation at the hot spots (Extended Fig. 2b and Supplementary Fig. 9). The porosity changes at all the hot-/cold-spot neighbourhoods for each cycle were tracked. The microstructure at these locations undergoes a noticeable change after numerous cycles (Extended Data Fig. 2c). The porosity change at the hot-/cold-spot neighbourhoods suggests that either Li metal is growing at these locations or a crack is forming (Supplementary Fig. 25).

Combining FF-HEDM and tomographic datasets can also enable mapping the grain-type (220/230) density in space (Fig. 5a).

Figure 5b demonstrates a top-down visual of three grain-specific hot and cold spots directly mapped onto a 230 grain density map (Fig. 5c). The 230 space group (light blue) only represents 3% of the total grains. Most of the mapped region is dark blue (220 space group). These maps confirm the co-location of the identified stress hot/cold spots and 230 space groups (Fig. 5c and Supplementary Figs. 26 and 27). This is better visualized by zooming into location A and location B (Fig. 5d). The distribution of 230 polymorph grains is strongly correlated with the grains identified as the hot/cold spot. Furthermore, an increase in the X-ray-transparent region is measured in the tomography data, which is indicative of filament growth and/or cracking of the solid electrolyte. Strong correlation between the two datasets (tomography and FF-HEDM) provides strong evidence that Li metal is present near the high- and low-stress regions (polymorph regions). A combined insight from the FF-HEDM and tomography data clearly highlight the role of trace secondary phases on the degradation pathways of garnet solid electrolytes.

Polymorphism of this nature is not necessarily present in all garnet-type LLZO electrolytes and may be restricted to doped LLZO systems[24]. However, the presence of a secondary phase contributes to the microstructural heterogeneity of the solid electrolyte. Microstructural heterogeneity in polycrystalline materials typically includes grains, grain misorientation, defects and pores. The secondary phases observed in this study demonstrate distinct properties that also lead to heterogeneity in mechanical stress and ionic transport response within the solid electrolyte. Evidence for such heterogeneities is clearly observed in materials including Al-doped LLZO, amorphous lithium thiophosphate (LPS) and annealed LPS-LiI (Supplementary Fig. 26)[5,8]. Microstructural heterogeneity in the form of pores or non-uniform microstructure has been attributed to distinct fracture patterns in sulfide solid electrolytes[13]. The origin of these heterogeneities as well as polymorphism could be related to processing (for example, milling, sintering and/or non-uniform densification). More studies are necessary to enable control over active and inactive microstructural heterogeneities that may evolve.
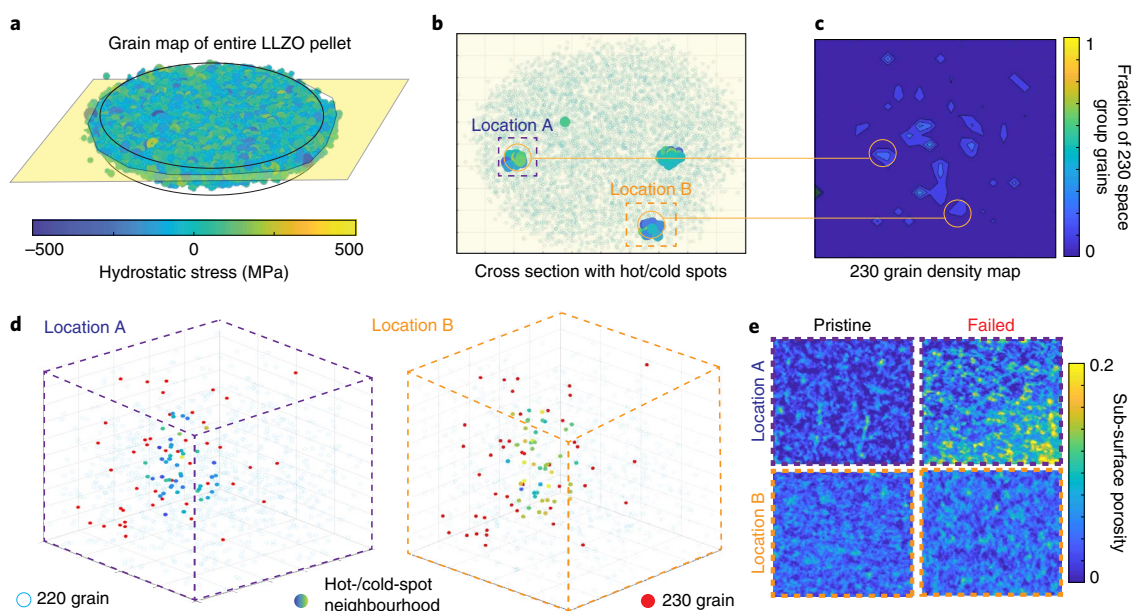
Fig. 5 | Correlating FF-HEDM and tomography datasets. a, Three-dimensional grain maps for the LLZO sample with the grain colour mapped to the hydrostatic stress values. The two circles are drawn over the scatter plot to facilitate visualization of the solid electrolyte shape. **b**, Cross-sectional map for a thin sub-volume within the bulk of the solid electrolyte as shown in the shaded plane in **a**, with hot/cold spots identified with filled markers. **c**, Correlating the location of the identified hot/cold spots with the spatial map of the 230 space group grain maps. The contour map represents the spatial 220 grain density within the identified sub-volume. **d**, Co-location of the hot-/cold-spot grains with the grains identified in the 230 polymorph and other 220 grains within a smaller sub-volume. A correlation between the spatial location of the 230 grains and the identified hot/cold spots is visualized. Note that these spatial maps are zoomed-in plots for the locations identified by the squares in **b**. **e**, Differences in sub-surface porosity for pristine and failed samples at the identified hot/cold spots in **b**.

Assessing stress-induced current flows

Stress within individual battery components and/or at interfaces can occur because of physical volume changes, formation of gas or mass transport. Although concentration gradients do not exist in a single-ion-conducting electrolyte, there is the potential for stress-assisted diffusion at solid–solid interfaces[48–50]. Recent modelling results have shown that mechanical stresses can alter the energy landscape for deposition and lead to conditions that promote localized electrodeposition[4]. Stress-induced current is correlated to the molar volume of the cation and results in ionic transport from regions of compressive stress to tensile stress. Experimental validation of this mechanism is extremely difficult because accessing spatially resolved stress fields within the bulk solid electrolyte is challenging. The stress identified by FF-HEDM measurements for individual grains enables us to assess the correlation between ion flow and stress gradient within the bulk solid electrolyte.

We consider electrodeposition at the working electrode as direction 1 and electrodissolution from the working electrode as direction 2 (Fig. 6a). Hydrostatic and von Mises stresses are identified and averaged over the hot-/cold-spot neighbourhoods from the FF-HEDM dataset for each electrochemical step. Subsequently, these values are plotted so that for each point on the graph, the initial-state configuration (pristine, plating-1, stripping-1, plating-2) is the x coordinate and the eventual-state configuration (plating-1, stripping-1, plating-2, stripping-2) is the y coordinate (Fig. 6b,c). This allows us to evaluate if the stress evolution has any correlation with the ion transport direction. Hydrostatic stress demonstrates a clear deviation between the two ion transport directions, whereas no directional separation was observed for von Mises stress. Hydrostatic stress represents the normal stress acting on the grains. Changes in hydrostatic stress based on the ion direction (stripping/plating) suggests interdependencies between material mechanics and mass transport in a solid electrolyte.

Directional, stress-assisted diffusion can lead to varying mechanical properties during cycling. Stress flow pathways were mapped from hot spots (Fig. 6d). Stress gradients or stress pathways were constructed by identifying the highest stress value and searching the closest grains for the lowest stress value (highest gradient). This continues until the pathway reaches a minimum stress. The normalized change in z position of the initial and final grain is defined as the stress neighbourhood relaxation (Fig. 6e). A positive value suggests that stress flows from the counter electrode to the working electrode, whereas a negative value indicates the opposite. This analysis was carried out over 50 grains and electrochemical cycling. The results show that on average, over multiple cycles, the stress flow direction favours transport in one direction compared with the other and the separation is stronger when the field current is along direction 1 compared with direction 2. These experiments provide further evidence of stress-assisted diffusion in solid electrolytes. Overall, polycrystalline materials that distribute hydrostatic stresses through numerous grains are more likely to experience stress-assisted diffusion than isotropic glassy materials.

This work couples FF-HEDM and tomography measurements to assess the grain-level chemo-mechanics in garnet solid electrolytes. Mechanical state mapping of all the grains in bulk solid electrolytes during electrochemical cycling indicates that failure in garnet solid electrolytes is initiated locally and is probably a stochastic process. The presence of a trace, secondary cubic polymorphic phase can lead to local transport and mechanical gradients within the solid electrolyte. We observe a strong correlation between stress hot and cold spots with the regions showing high microstructural variation and presence of a secondary cubic polymorph. The combination of real- and reciprocal-space imaging experiments provides evidence of a strong coupling between field-driven ion transport and the mechanical response of grains. Processing strategies that enable control over the powder properties and dopant transport
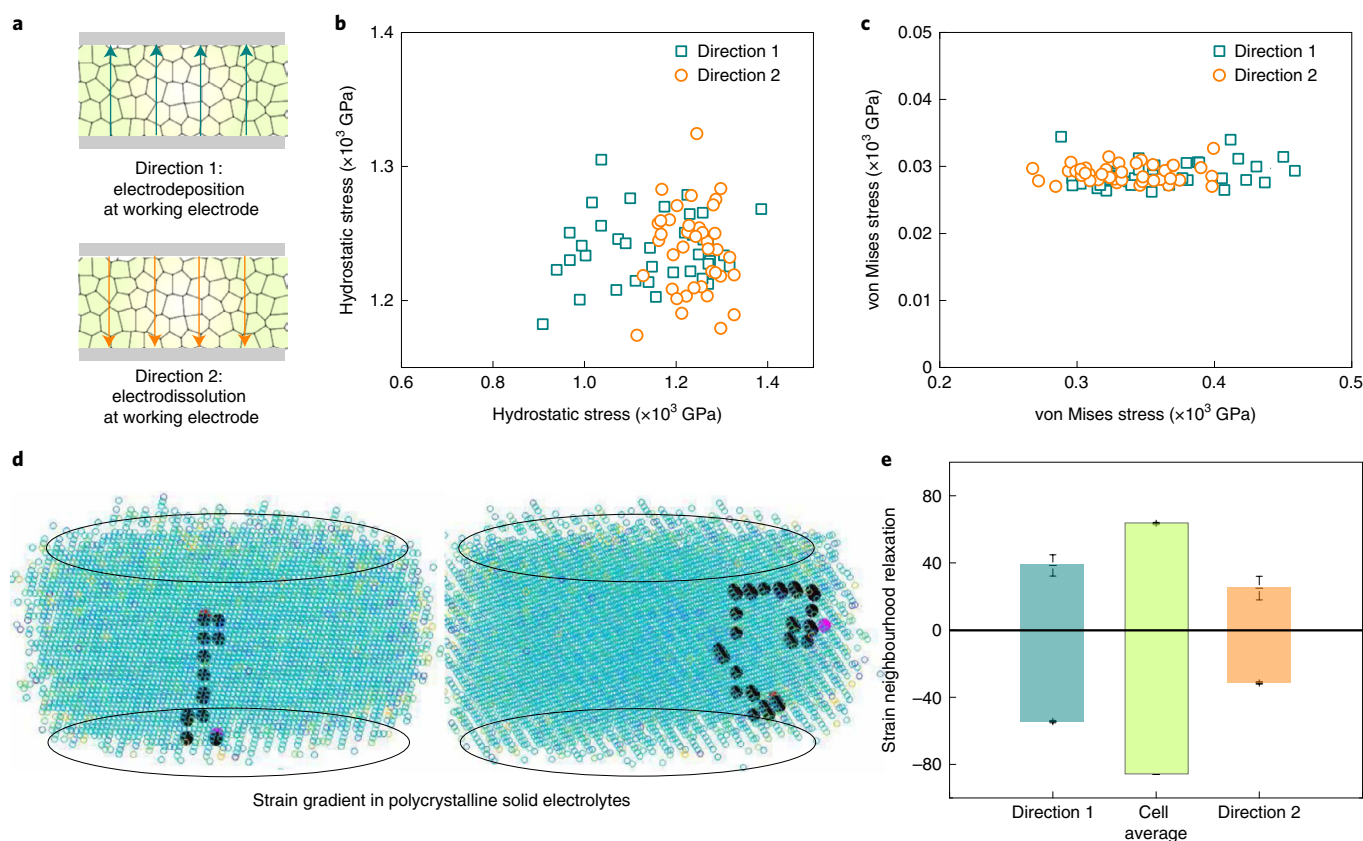
Fig. 6 | Evaluating stress flow directions in bulk solid electrolytes. a, Schematic showing the two ion current directions based on the applied electric field. **b,c**, Correlation between hydrostatic (**b**) and von Mises (**c**) stress of the grains separated as a function of the field direction. **d**, Stress flow pathways identified by the path of maximum gradient for stress within the sample. Here stress flow paths along the direction of the highest strain gradient are shown for two cases with distinct grains used as the initial grain. **e**, Average relaxation as a cell average and for the individual field directions. The relaxation is defined as the difference in the *z* position of the initial and final grain in the stress flow paths. Error bars capture range over 50 different grains.

are pathways to control the concentration and properties of polymorphs in solid electrolytes.

Online content

Any methods, additional references, Nature Research reporting summaries, source data, extended data, supplementary information, acknowledgements, peer review information; details of author contributions and competing interests; and statements of data and code availability are available at https://doi.org/10.1038/s41563-022-01333-y.

References

1. Krauskopf, T., Richter, F. H., Zeier, W. G. & Janek, J. Physicochemical concepts of the lithium metal anode in solid-state batteries. *Chem. Rev.* **120**, 7745–7794 (2020).
2. Randau, S. et al. Benchmarking the performance of all-solid-state lithium batteries. *Nat. Energy* **5**, 259–270 (2020).
3. Hatzell, K. B. et al. Challenges in lithium metal anodes for solid-state batteries. *ACS Energy Lett.* **5**, 922–934 (2020).
4. Mistry, A. & Mukherjee, P. P. Molar volume mismatch: a malefactor for irregular metallic electrodeposition with solid electrolytes. *J. Electrochem. Soc.* **167**, 082510 (2020).
5. Dixit, M. B., Park, J. S., Kenesei, P., Almer, J. & Hatzell, K. B. Status and prospect of in situ and operando characterization of solid-state batteries. *Energy Environ. Sci.* **14**, 4672–4711 (2021).
6. Lewis, J. A. et al. Linking void and interphase evolution to electrochemistry in solid-state batteries using operando X-ray tomography. *Nat. Mater.* **20**, 503–510 (2021).
7. Han, F. et al. High electronic conductivity as the origin of lithium dendrite formation within solid electrolytes. *Nat. Energy* **4**, 187–196 (2019).
8. Shen, F., Dixit, M. B., Xiao, X. & Hatzell, K. B. Effect of pore connectivity on Li dendrite propagation within LLZO electrolytes observed with synchrotron X-ray tomography. *ACS Energy Lett.* **3**, 1056–1061 (2018).
9. Kasemchainan, J. et al. Critical stripping current leads to dendrite formation on plating in lithium anode solid electrolyte cells. *Nat. Mater.* **18**, 1105–1111 (2019).
10. Swamy, T. et al. Lithium metal penetration induced by electrodeposition through solid electrolytes: example in single-crystal $Li_6La_3ZrTaO_{12}$ garnet. *J. Electrochem. Soc.* **165**, A3648 (2018).
11. Porz, L. et al. Mechanism of lithium metal penetration through inorganic solid electrolytes. *Adv. Energy Mater.* **7**, 1701003 (2017).
12. Wenzel, S., Sedlmaier, S. J., Dietrich, C., Zeier, W. G. & Janek, J. Interfacial reactivity and interphase growth of argyrodite solid electrolytes at lithium metal electrodes. *Solid State Ion.* **318**, 102–112 (2018).
13. Dixit, M. B. et al. In situ investigation of chemomechanical effects in thiophosphate solid electrolytes. *Matter* **3**, 2138–2159 (2020).
14. Wang, M. J., Choudhury, R. & Sakamoto, J. Characterizing the Li-solid-electrolyte interface dynamics as a function of stack pressure and current density. *Joule* **3**, 2165–2178 (2019).
15. Asano, T. et al. Solid halide electrolytes with high lithium-ion conductivity for application in 4 V class bulk-type all-solid-state batteries. *Adv. Mater.* **30**, 1803075 (2018).
16. Dawson, J., Famprikis, T. & Johnston, K. E. Anti-perovskites for solid-state batteries: recent developments, current challenges and future prospects. *J. Mater. Chem. A* **9**, 18746–18772 (2021).
17. Wang, A. N. et al. Mechanical properties of the solid electrolyte Al-substituted $Li_7La_3Zr_2O_{12}$ (LLZO) by utilizing micro-pillar indentation splitting test. *J. Eur. Ceram. Soc.* **38**, 3201–3209 (2018).
18. Fu, Z. et al. Probing the mechanical properties of a doped $Li_7La_3Zr_2O_{12}$ garnet thin electrolyte for solid-state batteries. *ACS Appl. Mater. Interfaces* **12**, 24693–24700 (2020).

19. Sharafi, A., Haslam, C. G., Kerns, R. D., Wolfenstine, J. & Sakamoto, J. Controlling and correlating the effect of grain size with the mechanical and electrochemical properties of $Li_7La_3Zr_2O_{12}$ solid-state electrolyte. *J. Mater. Chem. A* **5**, 21491–21504 (2017).

20. Kim, Y. et al. The effect of relative density on the mechanical properties of hot-pressed cubic $Li_7La_3Zr_2O_{12}$. *J. Am. Ceram. Soc.* **99**, 1367–1374 (2016).

21. El-Shinawi, H., Paterson, G. W., MacLaren, D. A., Cussen, E. J. & Corr, S. A. Low-temperature densification of Al-doped LLZO: a reliable and controllable synthesis of fast-ion conducting garnets. *J. Mater. Chem. A* **5**, 319–329 (2016).

22. Van Den Broek, J., Afyon, S. & Rupp, J. L. Interface-engineered all-solid-state Li-ion batteries based on garnet-type fast Li+ conductors. *Adv. Energy Mater.* **6**, 1600736 (2016).

23. Afyon, S., Krumeich, F. & Rupp, J. L. A shortcut to garnet-type fast Li-ion conductors for all-solid state batteries. *J. Mater. Chem. A* **3**, 18636–18648 (2015).

24. Rettenwander, D. et al. Structural and electrochemical consequences of Al and Ga cosubstitution in $Li_7La_3Zr_2O_{12}$ solid electrolytes. *Chem. Mater.* **28**, 2384–2392 (2016).

25. Krauskopf, T. et al. The fast charge transfer kinetics of the lithium metal anode on the garnet-type solid electrolyte $Li_{6.25}Al_{0.25}La_3Zr_2O_{12}$. *Adv. Energy Mater.* **10**, 2000945 (2020).

26. Sharafi, A., Meyer, H. M., Nanda, J., Wolfenstine, J. & Sakamoto, J. Characterizing the $Li–Li_7La_3Zr_2O_{12}$ interface stability and kinetics as a function of temperature and current density. *J. Power Sources* **302**, 135–139 (2016).

27. Cheng, L. et al. Effect of surface microstructure on electrochemical performance of garnet solid electrolytes. *ACS Appl. Mater. interfaces* **7**, 2073–2081 (2015).

28. Qi, Y., Ban, C. & Harris, S. J. A new general paradigm for understanding and preventing Li metal penetration through solid electrolytes. *Joule* **4**, 2599–2608 (2020).

29. Ma, C. et al. Interfacial stability of Li metal–solid electrolyte elucidated via in situ electron microscopy. *Nano Lett.* **16**, 7030–7036 (2016).

30. Park, K. et al. Electrochemical nature of the cathode interface for a solid-state lithium-ion battery: interface between $LiCoO_2$ and garnet-$Li_7La_3Zr_2O_{12}$. *Chem. Mater.* **28**, 8051–8059 (2016).

31. Brugge, R. H. et al. The origin of chemical inhomogeneity in garnet electrolytes and its impact on the electrochemical performance. *J. Mater. Chem. A* **8**, 14265–14276 (2020).

32. Yang, Y. et al. In situ electron holography for characterizing Li ion accumulation in the interface between electrode and solid-state-electrolyte. *J. Mater. Chem. A* **9**, 15038–15044 (2021).

33. Liu, X. et al. Local electronic structure variation resulting in Li 'filament' formation within solid electrolytes. *Nat. Mater.* **20**, 1485–1490 (2021).

34. Schuren, J. C. et al. New opportunities for quantitative tracking of polycrystal responses in three dimensions. *Curr. Opin. Solid State Mater. Sci.* **19**, 235–244 (2015).

35. Dixit, M. B. et al. Synchrotron imaging of pore formation in Li metal solid-state batteries aided by machine learning. *ACS Appl. Energy Mater.* **3**, 9534–9542 (2020).

36. Wang, M. & Sakamoto, J. Correlating the interface resistance and surface adhesion of the Li metal-solid electrolyte interface. *J. Power Sources* **377**, 7–11 (2018).

37. Park, J. S., Lienert, U., Dawson, P. R. & Miller, M. P. Quantifying three-dimensional residual stress distributions using spatially-resolved diffraction measurements and finite element based data reduction. *Exp. Mech.* **53**, 1491–1507 (2013).

38. Haeffner, D. R., Almer, J. D. & Lienert, U. The use of high energy X-rays from the Advanced Photon Source to study stresses in materials. *Mater. Sci. Eng. A* **399**, 120–127 (2005).

39. Birkbak, M. E. et al. Concurrent determination of nanocrystal shape and amorphous phases in complex materials by diffraction scattering computed tomography. *J. Appl. Cryst.* **50**, 192–197 (2017).

40. Martins, R. V., Ohms, C. & Decroos, K. Full 3D spatially resolved mapping of residual strain in a 316L austenitic stainless steel weld specimen. *Mater. Sci. Eng. A* **527**, 4779–4787 (2010).

41. Bernier, J. V., Barton, N. R., Lienert, U. & Miller, M. P. Far-field high-energy diffraction microscopy: a tool for intergranular orientation and strain analysis. *J. Strain Anal. Eng. Des.* **46**, 527–547 (2011).

42. Yu, S. et al. Elastic properties of the solid electrolyte $Li_7La_3Zr_2O_{12}$ (LLZO). *Chem. Mater.* **28**, 197–206 (2016).

43. Vishnugopi, B. S. et al. Mesoscale interrogation reveals mechanistic origins of lithium filaments along grain boundaries in inorganic solid electrolytes. *Adv. Energy Mater.* **12**, 2102825 (2022).

44. Vishnugopi, B. S., Hao, F., Verma, A. & Mukherjee, P. P. Double-edged effect of temperature on lithium dendrites. *ACS Appl. Mater. Interfaces* **12**, 23931–23938 (2020).

45. Ma, C. et al. Excellent stability of a lithium-ion-conducting solid electrolyte upon reversible Li+/H+ exchange in aqueous solutions. *Angew. Chem.* **127**, 131–135 (2015).

46. Cussen, E. J. Structure and ionic conductivity in lithium garnets. *J. Mater. Chem.* **20**, 5167–5173 (2010).

47. Yu, S. & Siegel, D. J. Grain boundary softening: a potential mechanism for lithium metal penetration through stiff solid electrolytes. *ACS Appl. Mater. Interfaces* **10**, 38151–38158 (2018).

48. Larson, J. M. et al. Pascalammetry with operando microbattery probes: sensing high stress in solid-state batteries. *Sci. Adv.* **4**, eaas8927 (2018).

49. Cannarella, J. et al. Mechanical properties of a battery separator under compression and tension. *J. Electrochem. Soc.* **161**, F3117 (2014).

50. Gor, G. Y., Cannarella, J., Prévost, J. H. & Arnold, C. B. A model for the behavior of battery separators in compression at different strain/charge rates. *J. Electrochem. Soc.* **161**, F3065 (2014).

Methods

Electrolyte, cell preparation and electrochemical testing. $Li_{6.5}La_3Zr_{1.5}Ta_{0.5}O_{12}$ was synthesized using a solid-state reaction process detailed previously[35,51]. Briefly, stoichiometric quantities of $LiOH$, La_2O_3, ZrO_2 and Ta_2O_5 were ball milled and sintered initially[52,53]. Subsequent to a secondary ball-milling cycle for size reduction, 3-mm-diameter pellets were pressed and sintered at 1,130 °C for 10 h (ref. [54]). The pellets were subsequently polished to a diameter of approximately 1.6 mm for synchrotron experiments. The pellets were sintered with excess mother powder for densification in an air atmosphere. There were no additional post-thermal/acid-etching steps before assembling the cell for critical current density measurements. The typical density of the measured pellets was 94–95% as measured from the tomography datasets for the entire pellet volume. The thickness of the pellets was in the range of 700–800 μm. Pellet thickness and local density variation did not contribute—in any meaningful way—to the locations of the secondary phase[55]. The maximum sample size is determined by the optics configuration, sample-detector distance, d-spacing range under investigation and beam energy. The ~2 mm size of the sample was optimized to provide high resolution for strain over the d-spacing range of interest in LLZO as well as enable Li-metal imaging[56]. In our earlier work, we discussed the role of experimental constraints and their impact on the cause of the relatively low values of the critical current density metrics measured under in situ conditions. Symmetric Li|LLZO|Li cells were assembled in an argon glove box at the Advanced Photon Source. The cell was loaded onto a special in situ cell to enable electrochemical testing as the diffraction and tomography experiments were being carried out. The typical interfacial resistance value for the cell was estimated at ~2,500 Ω cm² and the conductivity of the solid electrolyte was estimated to be ~5 × 10⁻⁴ mS cm⁻¹. Galvanostatic plating/stripping tests were carried out on Li|LLZO|Li symmetric cells at increasing current densities until the short-circuit value of the cell was observed. Electronic impedance spectroscopy was carried out between 1 MHz and 100 mHz with a 50 mV amplitude. Impedance measurements were taken after individual plating and stripping cycles.

FF-HEDM and tomography measurements. FF-HEDM experiments were carried out at the 1-ID-E beamline of the Advanced Photon Source at the Argonne National Laboratory (Supplementary Fig. 1)[57]. Experimental conditions for LLZTO were identified with optimum energy and sample-detector distance of 76.2 keV and 2.189 m, respectively. In a typical FF-HEDM experiment, the sample was rotated from −180.0 to 180.0° with respect to the incoming X-rays at 0.1° steps. Diffraction images were captured on a two-dimensional area detector (GE-41RT, 2,048 × 2,048 pixels, 200 μm pitch) with 1 s exposure time. FF-HEDM used a box beam of 100 μm height and hence the scan for the entire Li|LLZO|Li cell was completed in over nine sections. The acquisition time for a single FF-HEDM scan of the entire LLZO cell was roughly 1.5 h. Initially, a pristine LLZO cell was characterized with FF-HEDM to assess the initial stress configuration. Subsequently, in situ testing was carried out for symmetric cells at the end of each plating and stripping step. Tomography on the symmetric cell was also carried out on the cell at interim locations where FF-HEDM scans were taken. Details of the tomography experiment are reported previously[35] and details regarding the diffraction analysis are included in the Supplementary Information (refs. [58,59]).

Synchrotron XRD measurements. High-resolution XRD patterns were collected from the LLZO pellet at the 1-ID-E beamline. Spatially resolved XRD patterns were collected with a resolution of 0.1 mm. Diffraction was recorded during 180° rotation of the sample with an exposure time of 0.2 s. The diffraction patterns were recorded on the PILATUS CdTe detector, which has a dynamic range of 2 × 10²⁰ and a maximum radial dispersity of 100:1. The high dynamic range of the detector allows the capture of diffraction peaks with very low structure factors.

Computational methods. *Kinetic Monte Carlo model.* Ion transport behaviour in the vicinity of the interface between the bulk and foreign solid electrolyte phases has been captured using a kinetic Monte Carlo modelling approach.

First, transport rate constants, k_{T1} and k_{T2}, are defined based on the ion migration barriers, namely, E_{a1} and E_{a2} in the bulk and secondary phases of the solid electrolyte, respectively. The rate of ion migration from one lattice site to another is calculated according to the Arrhenius equation.

$$k_{Ti} = \nu \exp\left(\frac{-E_{ai}}{k_B T}\right) \quad [i = 1, 2]. \tag{1}$$

Here ν is the hopping frequency, T is the temperature and k_B is the Boltzmann constant.

The total rate constant k_{total} is calculated as follows:

$$k_{total} = \sum_{i=1}^{N_1} k_{T1}^i + \sum_{j=1}^{N_2} k_{T2}^j, \tag{2}$$

where N_1 and N_2 represent the total number of ions inside the bulk and foreign phases of the solid electrolyte, respectively. Subsequently, random number r_1 is chosen between 0 and 1. All the possible ion migration events in the system are sequentially scanned, and the first event for which the total rate of the previously scanned events is larger than $k_{total}r_1$ is selected. The system is then evolved based on the chosen ion transport event. Simulations have been carried out until a total of 4×10^8 ion migration events have been completed. The simulated system is 60 nm × 60 nm, with the foreign phase occupying a 7 nm × 60 nm region in the middle of the domain. The remainder of the domain is occupied by the bulk solid electrolyte phase. The initial ion occupancy is set to 2% throughout the domain.

Mechanics model. To capture the stress state of the system, the governing equation for mechanical stress assuming quasi-static mechanical equilibrium is solved:

$$\nabla \cdot \boldsymbol{\sigma} = 0. \tag{3}$$

The top and bottom boundaries of the solid electrolyte and Li metal, respectively, are subjected to a constant external pressure, namely, $\boldsymbol{\sigma}\mathbf{n} = P_{ext}\mathbf{n}$. The left and right boundaries of the solid electrolyte and Li metal are fixed in the normal direction. An external pressure of 1 MPa is applied and linear elasticity is assumed for the Li metal and solid electrolyte:

$$\boldsymbol{\sigma} = \frac{E}{1+\nu}\boldsymbol{\varepsilon} + \frac{\nu E}{(1+\nu)(1-2\nu)}\text{trace}(\boldsymbol{\varepsilon})\mathbf{I}. \tag{4}$$

Here $\boldsymbol{\sigma}$ and $\boldsymbol{\varepsilon}$ correspond to the stress and strain tensors, respectively. Young's modulus (E) of Li is taken to be 7.8 GPa, whereas Young's moduli of the bulk and foreign phases of LLZO are assumed to be 161 and 156 GPa, respectively. The Poisson ratios (ν) of Li and LLZO are considered to be 0.38 and 0.27, respectively.

Dimensions of the described domain have been represented in a schematic (Supplementary Fig. 17); the stress state of the dotted region, present away from the interface and consisting of the bulk phase (with the embedded secondary phase), has been plotted earlier. Secondary phases, possessing distinct mechanical properties, are assumed to be 30 μm in radius, comparable to the measured grain size in the samples. Coordinates of the centres of circles c_1, c_2 and c_3 (Fig. 1) are (480 μm, 420 μm), (330 μm, 150 μm) and (120 μm, 330 μm), respectively. For simplicity, circular 230 domains (60 μm in diameter) were assumed within a bulk 220 phase (Supplementary Fig. 9). The 230 space group has an ionic conductivity of around 0.3 mS cm⁻¹ and the 220 polymorph has an ionic conductivity of around 1 mS cm⁻¹ (ref. [24]). Since limited data are available on the mechanical properties of these two cubic polymorphs of LLZO, a 3% variation in Young's modulus was assumed in the mechanical simulations. Although a larger variation may lead to a quantitatively different stress profile, it is noted that the mechanical response trends in the vicinity of the secondary phase would still remain similar.

Electrochemical transport model. The electric potential in the solid electrolyte system is obtained by solving the following governing equation:

$$\nabla \cdot (k_{SE}\nabla\phi_e) = 0. \tag{5}$$

Here ϕ_e represents the electric potential and k_{SE} represents the ionic conductivity of the solid electrolyte.

At the Li–electrolyte interface, electrochemical reactions following the Butler–Volmer kinetics occur: $-k_{SE}\nabla\phi_e = i_0\left(\exp\left(\frac{\alpha_a F}{RT}\eta\right) - \exp\left(-\frac{\alpha_c F}{RT}\eta\right)\right)$. Here i_0 is the exchange current density, F is the Faraday constant, R is the gas constant, T is the temperature, α_a and α_c are the charge transfer coefficients, and η is the kinetic overpotential. Due to the high electronic conductivity of Li metal, the potential drop in the Li-metal domain has been neglected in the calculations. Current density ($i_{app} = 0.5$ mA cm⁻²) is applied at the top boundary of the solid electrolyte, that is, $-k_{SE}\nabla\phi_e = i_{app}$. The left and right boundaries are set to $\nabla\phi_e \cdot \mathbf{n} = 0$.

The electric potential distribution at the vicinity of the secondary phase region located at (330 μm, 150 μm) has been presented in the manuscript.

Data availability

Data presented in this study are available from the corresponding authors upon request.

References

51. Bernuy-Lopez, C. et al. Atmosphere controlled processing of Ga-substituted garnets for high Li-ion conductivity ceramics. *Chem. Mater.* **26**, 3610–3617 (2014).
52. Tan, J. & Tiwari, A. Synthesis of cubic phase $Li_7La_3Zr_2O_{12}$ electrolyte for solid-state lithium-ion batteries. *Electrochem. Solid-State Lett.* **15**, A37 (2011).
53. Hatzell, K. B. & Zheng, Y. Prospects on large-scale manufacturing of solid state batteries. *MRS Energy Sustain.* **8**, 33–39 (2021).
54. Fritsch, C. et al. Garnet to hydrogarnet: effect of post synthesis treatment on cation substituted LLZO solid electrolyte and its effect on Li ion conductivity. *RSC Adv.* **11**, 30283–30294 (2021).
55. Wagner, R. et al. Crystal structure of garnet-related Li-ion conductor $Li_{7-3x}Ga_xLa_3Zr_2O_{12}$: fast Li-ion conduction caused by a different cubic modification? *Chem. Mater.* **28**, 1861–1871 (2016).

56. Zhao, L. et al. Laplace-Fourier transform solution to the electrochemical kinetics of a symmetric lithium cell affected by interface conformity. *J. Power Sources* **531**, 231305 (2022).
57. Li, R. et al. Unveiling the origins of work-hardening enhancement and mechanical instability in laser shock peened titanium. *Acta Mater.* **229**, 117810 (2022).
58. Nielsen, S. F. et al. A conical slit for three-dimensional XRD mapping. *J. Synchrotron Rad.* **7**, 103–109 (2000).
59. Suter, R. M., Hennessy, D., Xiao, C. & Lienert, U. Forward modeling method for microstructure reconstruction using X-ray diffraction microscopy: single-crystal verification. *Rev. Sci. Instrum.* **77**, 123905 (2006).

Acknowledgements

Author contributions

M.B.D. and K.B.H. conceived the concept and idea. M.B.D. and W.Z. performed the synchrotron imaging and diffraction experiments. J-S.P., J.A. and P.K. performed the synchrotron measurements and helped with the analysis. M.B.D. completed the image processing and analysis from the synchrotron experiments. B.S.V. and P.P.M. carried out the modelling efforts. M.D. and K.B.H. wrote the manuscript. The manuscript was edited by all the authors.

Competing interests

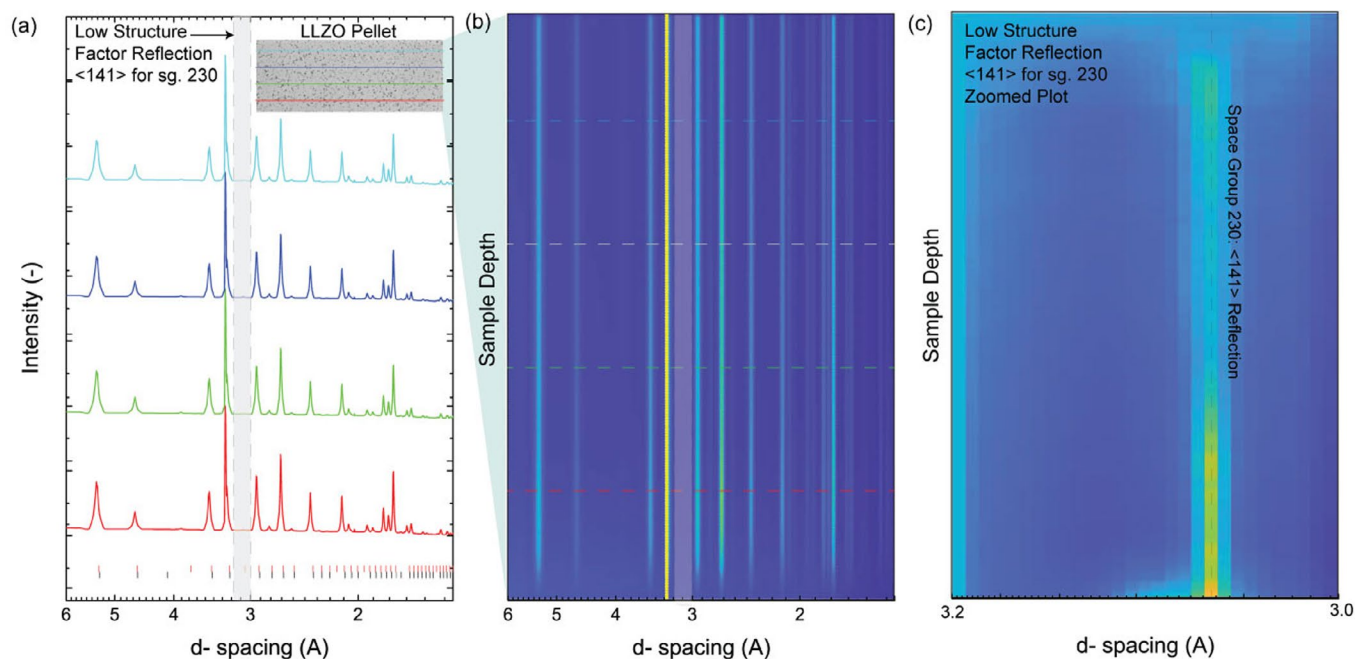The authors declare no competing interests.

Additional information

Extended data is available for this paper at https://doi.org/10.1038/s41563-022-01333-y.

Supplementary information The online version contains supplementary material available at https://doi.org/10.1038/s41563-022-01333-y.
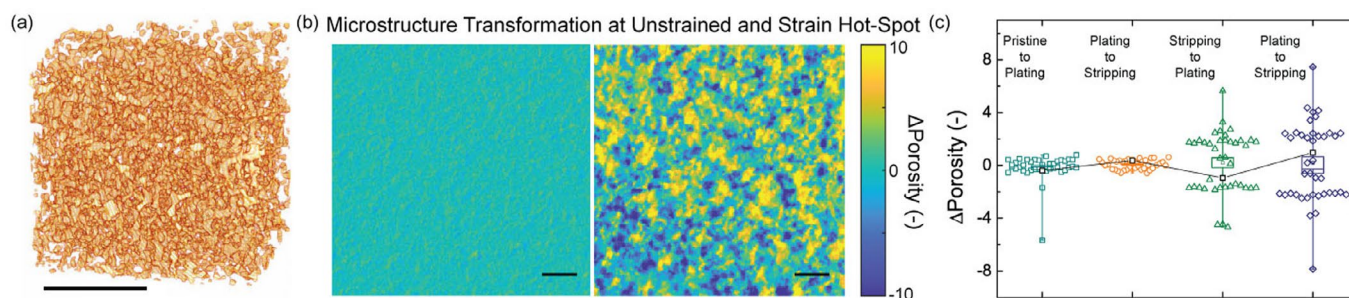
Correspondence and requests for materials should be addressed to Marm B. Dixit or Kelsey B. Hatzell.

Peer review information *Nature Materials* thanks Marca Doeff, Ainara Aguadero and the other, anonymous, reviewer(s) for their contribution to the peer review of this work.

Reprints and permissions information is available at www.nature.com/reprints.

Extended Data Fig. 1 | Evaluating the presence of trace phases in sintered LLZO pellets. (a) High resolution, X-Ray diffraction patterns from specified locations of an LLZO pellet. (b) Spatially resolved high resolution XRD map of the LLZO pellet. (c) Spatially resolved XRD map zoomed to the anticipated location of the low-structure factor peak corresponding to <141> plane in the 230 space group LLZO.

Extended Data Fig. 2 | Correlating grain-level mechanics to the bulk microstructure. (a) Difference in the pore structure of a hot-spot neighbourhood between the pristine and the failed sample. The structure represents the modification of pore network between pristine and the failed sample. The scale bar in the figure is 100 μm (b) Depth averaged Δporosity values for identical sub-volume sizes taken at a hot spot region (right) and other (unstrained) regions of the bulk pellet. The porosity difference is calculated between the pristine and the failed sample. The scale bar in the figure is 10 μm. (c) Difference in porosity values tracked over the hot-spot and cold-spots for each step plotted as a box plot. Additionally, the average porosity difference over the entire pellet between each step is overlayed and connected by a solid line. As the sample undergoes degradation with cycling, the hot-/cold-neighbourhoods clearly show very high variance in the porosity change compared to the bulk sample value.